**RESEARCH**

# Integrating image processing and deep learning for effective analysis and classification of dust pollution in mining processes

JiangJiang Yin[1] · Jiangyang Lei[1] · Kaixin Fan[1] · Shaofeng Wang[1] 📧

## Abstract
A comprehensive evaluation method is proposed to analyze dust pollution generated in the production process of mines. The method employs an optimized image-processing and deep learning framework to characterize the gray and fractal features in dust images. The research reveals both linear and logarithmic correlations between the gray features, fractal dimension, and dust mass, while employing Chauvenel criteria and arithmetic averaging to minimize data discreteness. An integrated hazardous index is developed, including a logarithmic correlation between the index and dust mass, and a four-category dataset is subsequently prepared for the deep learning framework. Based on the range of the hazardous index, the dust images are divided into four categories. Subsequently, a dust risk classification system is established using the deep learning model, which exhibits a high degree of performance after the training process. Notably, the model achieves a testing accuracy of 95.3%, indicating its effectiveness in classifying different levels of dust pollution, and the precision, recall, and F1-score of the system confirm its reliability in analyzing dust pollution. Overall, the proposed method provides a reliable and efficient way to monitor and analyze dust pollution in mines.

## 1 Introduction

The generation of dust is a pervasive issue in industrial production worldwide, particularly in mining processes (Liu and Liu 2020). During mining operations, rocks and minerals are subjected to various stresses such as drilling, cutting, crushing, and grinding, resulting in the reduction of particle size and the generation of substantial dust pollution (Chen et al. 2018). In recent years, due to the depletion of surface ore reserves, mining production has shifted towards deep underground operations, with some mines reaching depths exceeding one kilometer (Cai 2019; Chen et al. 2019). This shift poses challenges in creating an ideal ventilation environment due to factors such as high ground stress, high ground temperature, high karst water pressure, and significant disturbances during excavation (He 2009), ultimately leading to a significant increase in dust pollution. Furthermore, in response to the growing demand for

mineral production, mines have increasingly adopted heavy mechanization, exacerbating dust generation (Zhang et al. 2018; Zhou and Zhang et al. 2017).

It is widely confirmed that high-concentration dust pollution poses significant risks to individuals working in and around mines (Bao et al. 2020; Fan and Liu 2021; Tan et al. 2020; Zhou and Fan et al. 2017). The fine particles generated during mining operations can be inhaled, leading to lung damage, respiratory diseases, and other health problems (Shekarian et al. 2021; Hill et al. 2023). Moreover, mining dust can create a fire or explosion hazard, especially in underground mining operations where flammable gases may be present (Valiulin et al. 2020). Additionally, the substantial amount of dust pollution has the potential to cause vegetation degradation and the destruction of animal habitats (Conesa et al. 2006). Consequently, the implementation of effective dust control measures, including ventilation, water sprays, and dust suppression chemicals, is crucial to minimizing the risks associated with mining dust (Ji et al. 2016; Wang et al. 2017). Regular monitoring of dust levels and worker health is also imperative to ensure a safe working environment.

📧 Shaofeng Wang
sf.wang@csu.edu.cn

[1] School of Resources and Safety Engineering, Central South University, Changsha 410083, Hunan, China

Currently, mining dust monitoring methods involve a combination of traditional and modern techniques. Traditionally, personal and area sampling methods have been used to monitor dust levels in mining environments (Tong et al. 2019). These methods require collecting air samples on filters or cassettes, which are later analyzed in a laboratory for dust content. Although these methods provide accurate measurements, they are time-consuming, and results may not be available for several days. In recent years, real-time monitoring methods have been developed, allowing for immediate feedback on dust levels in the workplace (Cyrys et al. 2001; Lépy et al. 2010). These methods typically involve the use of direct-reading instruments, such as photometers or laser-based sensors, that continuously measure dust concentrations (Miguel et al. 2015; Zhang et al. 2021). These instruments are portable and enable quick identification of areas with high dust levels and assessment of the effectiveness of dust control measures. However, these methods face challenges such as limited measurement range, bulky equipment, and insufficient accuracy. Moreover, these devices often require meticulous calibration procedures and specialized proficiency for operation by miners.

Digital image processing and deep learning techniques have demonstrated their effectiveness in various engineering applications due to several advantages over traditional monitoring methods, including non-invasiveness and reduced equipment requirements (Albatayneh et al. 2019; Fu and Wang 2013; Grasa and Abanades 2001; Lim 1993; Li et al. 2019; Shirmohammadi and Ferrero 2014). Regarding dust pollution, digital image processing methods typically involve analyzing images captured by cameras placed in mining environments to identify dust particles and estimate their concentration. These methods enable real-time monitoring of dust levels and provide a more comprehensive perception of dust dispersion in the workplace. For example, a proposed image method primarily demonstrated a logarithmic correlation between powdery dust volume fractions and image grayscale values, eliminating the need for fitting constants (Grasa and Abanades 2001). Likewise, a model utilized a mean grayscale value threshold to distinguish different brightness levels of powdery dust (Obregón and Velázquez 2007). The model then optimized the grayscale feature to estimate dust concentration based on the detected brightness differences. There are also studies that analyze the gray average and fractal dimension of dust images to determine the degree of dust pollution in simulation experiments and the diffusion law of smoke-dust in surface blasting (Wang et al. 2022; Yin et al. 2022). Notably, most existing researches were conducted in fluidized bed environments, where experiment images were collected and prepared for subsequent calculations. In addition, deep learning techniques, such as convolutional neural networks (CNNs), have been employed to improve the accuracy of dust detection and estimation. Existing methods involve training models on large datasets of images to recognize and classify different types of dust particles and estimate dust concentrations. For instance, a hybrid machine-learning technique was employed to predict PM concentration (Qi et al. 2020). Similarly, a model based on a multi-layer artificial neural network and fuzzy cognitive map was developed to predict blast-induced dust emissions in vertical and horizontal directions (Hosseini et al. 2021).

This paper presents a vision model that aims to recognize dust dispersion, analyze the relationship between image properties and dust mass, and classify dust pollution risks. The model is developed using an optimized image processing method that utilizes grayscale average and fractal dimension theory, along with a CNN model for image classification. To generate image data, a self-designed dust dispersion simulation system is employed. Statistical methods and arithmetic averaging are utilized for parameter calculations to reduce data discreteness. Subsequently, the CNN model is trained based on the dataset obtained through image processing. Ultimately, the proposed evaluation system, which combines digital image processing and a deep learning framework, can be utilized to implement preventative and emergency measures to protect individual health and property.

## 2 Methodology

### 2.1 Image processing algorithm for dust recognition

Particle feature extraction from digitized images can be challenging due to pixel-value differences. To distinguish dust particles from the background, high-quality dust image data is essential by developing related hardware and software. Then, an image processing algorithm based on pixel-gradient calculation was proposed to improve dust recognition. The detailed procedures of the algorithm are outlined below and illustrated in Fig. 1.

(1) Import and prepare images.

Original images of dust dispersion are imported into the computer and processed using specialized software and self-coded programs. The images are represented as three-dimensional digital matrices ($D_{(w \times h \times 3)}$), as shown in Eq. (1), where each pixel value ($d_{(i,j,k)}$) corresponds to a position in the image ($i, j$) and color channel ($k = 1, 2, 3$).

$$D_{(w \times h \times 3)} = \left[ d_{(i,j,k)} \right] \tag{1}$$

**Fig. 1** Flowchart of the image-processing operations for acquiring particle features
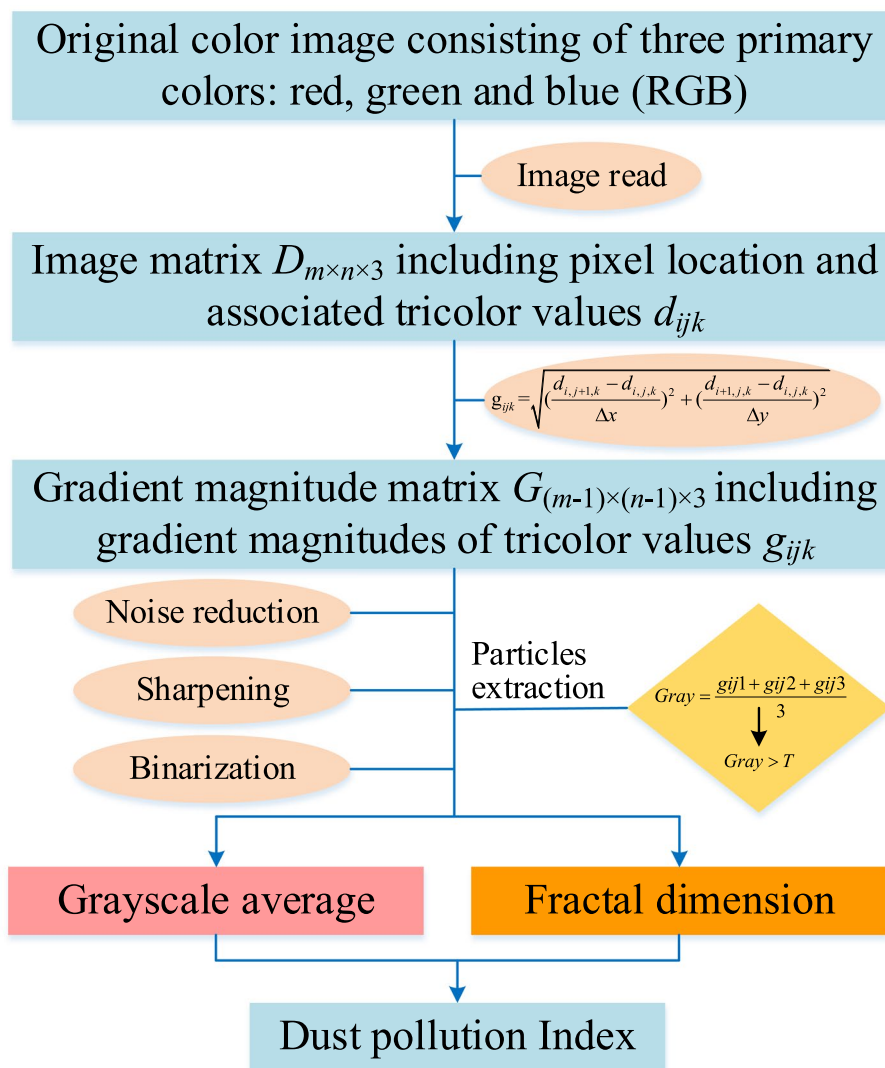


(2) Pixel-gradient calculation:

The proposed method employs pixel-gradient calculation (Eq. (2)) to enhance pixel contrast between particles and the background. This technique aids in segmenting boundary information and removing internal pixels of coarse dust particles. The resulting gradient matrix ($G_{(w \times h \times 3)}$), as shown in Eq. (3), is computed using differential steps ($\Delta x$, $\Delta y$) of one pixel unit.

$$g_{(i,j,k)} = \sqrt{\left(\frac{d_{(i,j+\Delta x,k)} - d_{(i,j,k)}}{\Delta x}\right)^2 + \left(\frac{d_{(i+\Delta y,j,k)} - d_{(i,j,k)}}{\Delta y}\right)^2} \tag{2}$$

$$G_{(w \times h \times 3)} = \left[g_{(i,j,k)}\right] \tag{3}$$

where $g_{(i,j,k)}$ is the gradient magnitude of a single pixel. $\Delta x$, $\Delta y$ represent the differential steps for searching the next pixel in different rows and columns, respectively.

(3) Binarization and image sharpening.

To separate particles from the background, binarization is performed. Before this step, noise reduction and image sharpening are carried out. Opening-denoising eliminates isolated pixels in the gradient images using a $3 \times 3$ window, while image sharpening enhances contrast. Binarization is employed based on a selected binary threshold (Eqs. (4) and (5)).

$$gray_{(i,j)} = \frac{g(i,j,1) + g(i,j,2) + g(i,j,3)}{3} \tag{4}$$

$$b_{(i,j)} = \begin{cases} gray_{(i,j)} = 1 \ gray_{(i,j)} > T \\ gray_{(i,j)} = 0 \ gray_{(i,j)} \leq T \end{cases} \tag{5}$$

where $gray_{(i,j)}$ represents the mean of gradient magnitude of the three-color channel, and $T$ is the selected binary threshold.

(4) Grayscale average (GA) and Fractal dimension (DF).

The grayscale average (GA) (Eq. (6)) is calculated to assess the overall gray level of the image and obtain the grayscale features of dust particles. The GA represents the proportion of pixels indicating particles to the total pixels in the entire image.

$$GA = \frac{\sum_i^h \sum_j^w b_{(i,j)}}{h \times w} \tag{6}$$

Then, the fractal dimension (DF) of dust particles is computed using Eq. (7), and the two-dimensional box-counting method is employed to fulfill the DF calculation. The image is covered by a series of square boxes with different sizes ($\delta = 1, 2, \dots, n$). For each box, record its side length ($\delta$) and the number of boxes ($N(\delta)$) where pixels denoting dust particles distribute. Then, take the logarithm of $N(\delta)$ and $1/\delta$, plot the data on a logarithmic coordinate system, and perform linear fitting. The resulting slope (DF) represents the fractal dimension of the dust image.

$$\ln(N(\delta)) = \mathrm{DF} \ln\left(\frac{1}{\delta}\right) + C \tag{7}$$

where $C$ denotes a regressed constant.

GA and DF parameters analyze the global and local distribution features of dust particles, respectively. GA provides a global view considering all pixels, while DF focuses on the complexity of dust-particle distribution, capturing local features of dust pixels.

## 2.2 Algorithm applicability of the proposed image-processing method

To further illustrate the effectiveness of the proposed image-processing method for dust particles and other particle-like phenomena, an image example of fugitive dust emission is employed to visually demonstrate the implementation processes of the algorithm. Figure 2 provides a detailed description of these processes.

In Fig. 2, an image of fugitive dust (Fig. 2a) with a size of $1536 \times 1025$ pixels was inputted into the computer, in which the image background is a relatively simple dark color while the particles exhibit a bright grayish-white color. By performing gradient calculations, particle features, especially for the boundary lines that differentiate from the

image background, are ulteriorly reinforced. The resulting processed image is shown in Fig. 2b. Furthermore, a distribution nephogram (Fig. 2c) is employed to visualize the dust diffusion, revealing distinct pixel differences between the particles and the surrounding background. Following noise reduction, sharpening, and binarization operations, the algorithm successfully identifies dust particles to a certain extent, as depicted in Fig. 2d. Subsequently, the grayscale features are analyzed, and a grayscale average distribution is obtained using a horizontal ergodic window (Fig. 2e) with a size of $10 \times 1025$ pixels. The calculation also records the pixel numbers representing dust particles. The resulting grayscale features are shown in Fig. 2g, with the grayscale average of the fugitive dust image measured at 0.3548. In addition, the dust image is divided into multiple two-dimensional boxes (Fig. 2f), and the fitted equation is calculated according to Eq. (8), with a goodness-of-fit ($R^2$) of 0.99:

$$\ln(N(\delta)) = 1.9289 \ln\left(\frac{1}{\delta}\right) - 0.2153 \tag{8}$$

From the grayscale and fractal parameters of the provided image example, it is evident that the fractal dimension (1.9289/2) exhibits a higher value compared to the grayscale average (0.3548/1). This disparity indicates the presence of pronounced fractal features in the image. Consequently, this observation validates that the image primarily manifests local characteristics rather than global features from a distinct perspective.

## 2.3 Deep learning framework based on the InceptionV3 model

A transfer learning method based on the InceptionV3 model is proposed to extract detailed particle features. The Inception model has won the ILSVRC international competition with a top-5 error rate of 6.67%, outperforming the other state-of-the-art image classification algorithm. The proposed model primarily incorporates inception modules to strike a balance between network width and depth, demonstrating superior performance in a wide range of computer vision tasks (Albatayneh et al. 2020; Liang et al. 2021). This not only enhances the accuracy of the model when dealing with complex images but also significantly reduces the number of parameters even when learning intricate representations, and enables the model to extract both local and global features effectively, assisting in accurately characterizing the dust features in sample images. Simultaneously, unlike other versions, the InceptionV3 model excels in the local processing of high-dimensional representations. A schematic diagram of the InceptionV3-based model is shown in Fig. 3.
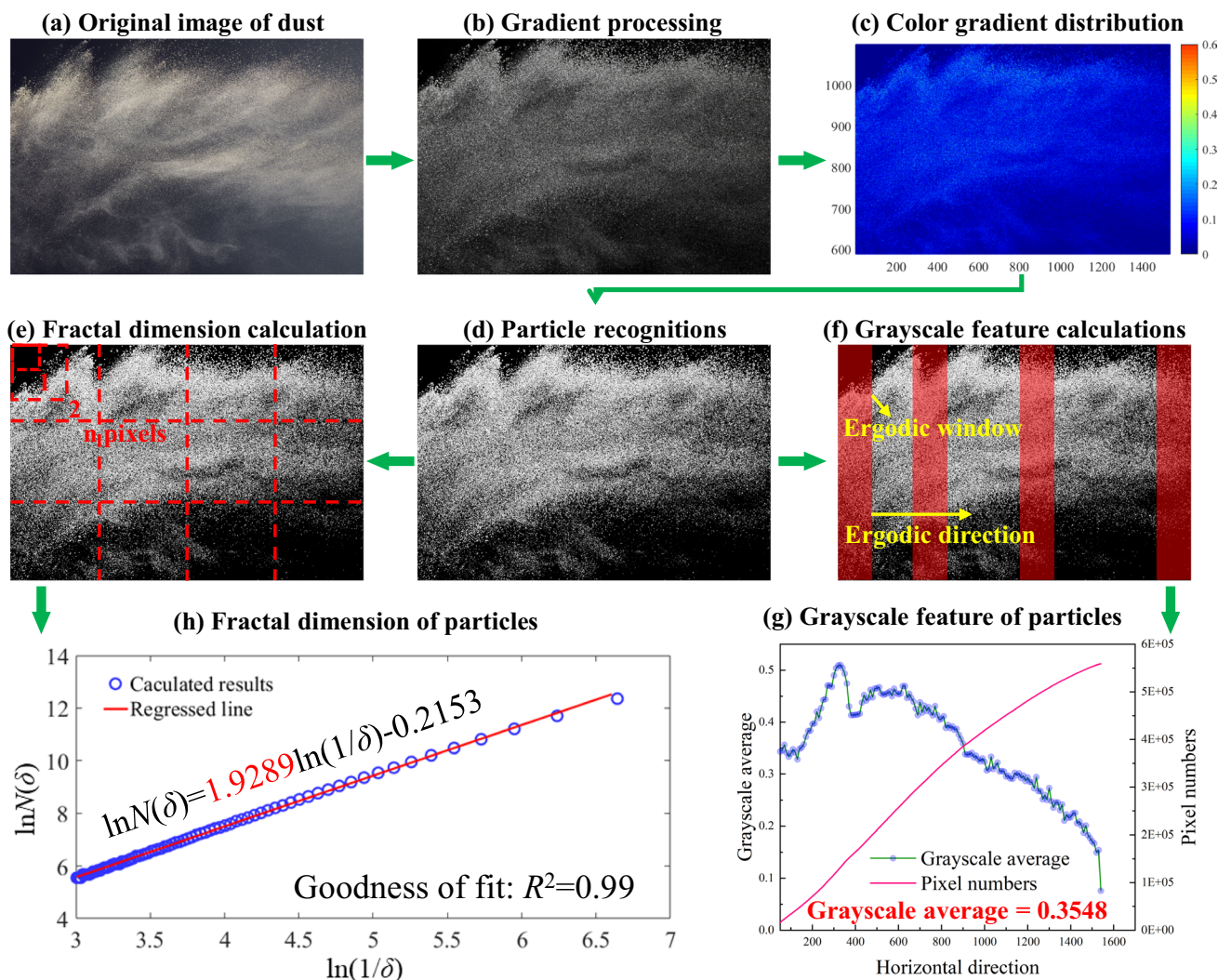
**(a) Original image of dust**

**(b) Gradient processing**

**(c) Color gradient distribution**

**(e) Fractal dimension calculation**

**(d) Particle recognitions**

**(f) Grayscale feature calculations**

Ergodic window

Ergodic direction

**(h) Fractal dimension of particles**

$\ln N(\delta) = 1.9289\ln(1/\delta) - 0.2153$

Goodness of fit: $R^2 = 0.99$

- Caculated results
- Regressed line

**(g) Grayscale feature of particles**

Grayscale average = 0.3548

- Grayscale average
- Pixel numbers

**Fig. 2** Description of the proposed image-processing method for identifying the grayscale and fractal features of fugitive dust emission, including **a** The original image of fugitive dust emission, **b** The gradient image, **c** The color gradient distribution, (**d**) the binarization result of particle recognitions, **e**, **f** The calculation processes of grayscale and fractal features, and **g**, **h** The grayscale-average distribution and fractal dimension of dust particles

The overall network architecture, as depicted in Fig. 3a, consists of 47 layers and 12 modules, in which there are 106 convolutional layers, 16 pooling layers, 1 softmax layer and 2 fully connected layers. Notably, the inception modules (inception A, inception B, and inception C) shown in Fig. 3b play a crucial role in enhancing the efficiency and accuracy of the model. These modules facilitate the network in learning complex and multi-scale patterns by incorporating filters of various sizes and parallel pooling operations. As a result, the network can capture both fine-grained and coarse features, thereby improving performance in tasks such as image classification.

Once a training dataset is fed into the network, which comprises a certain number images with the size of $H_c$, $W_c$ and $C_c$ shown as Fig. 3c, the network learns the inner features through a series of convolutional computations and global average pooling. This process can be described using the following formulas:

$$C_{W,b}^{l+1}(x,y) = \sum_{k=1}^{3} \sum_{j=1}^{n} \sum_{i=1}^{m} W_{i,j,k}^{l+1} \cdot I^l(x+i-1, y+j-1, k) + bs \tag{9}$$

$$p^{l+1}(x,y) = \frac{\sum_{(p,q\in R)} x(p,q)}{|R|} \tag{10}$$

**(a) Model structure**      **(b) Inception module**      **(c) System application**
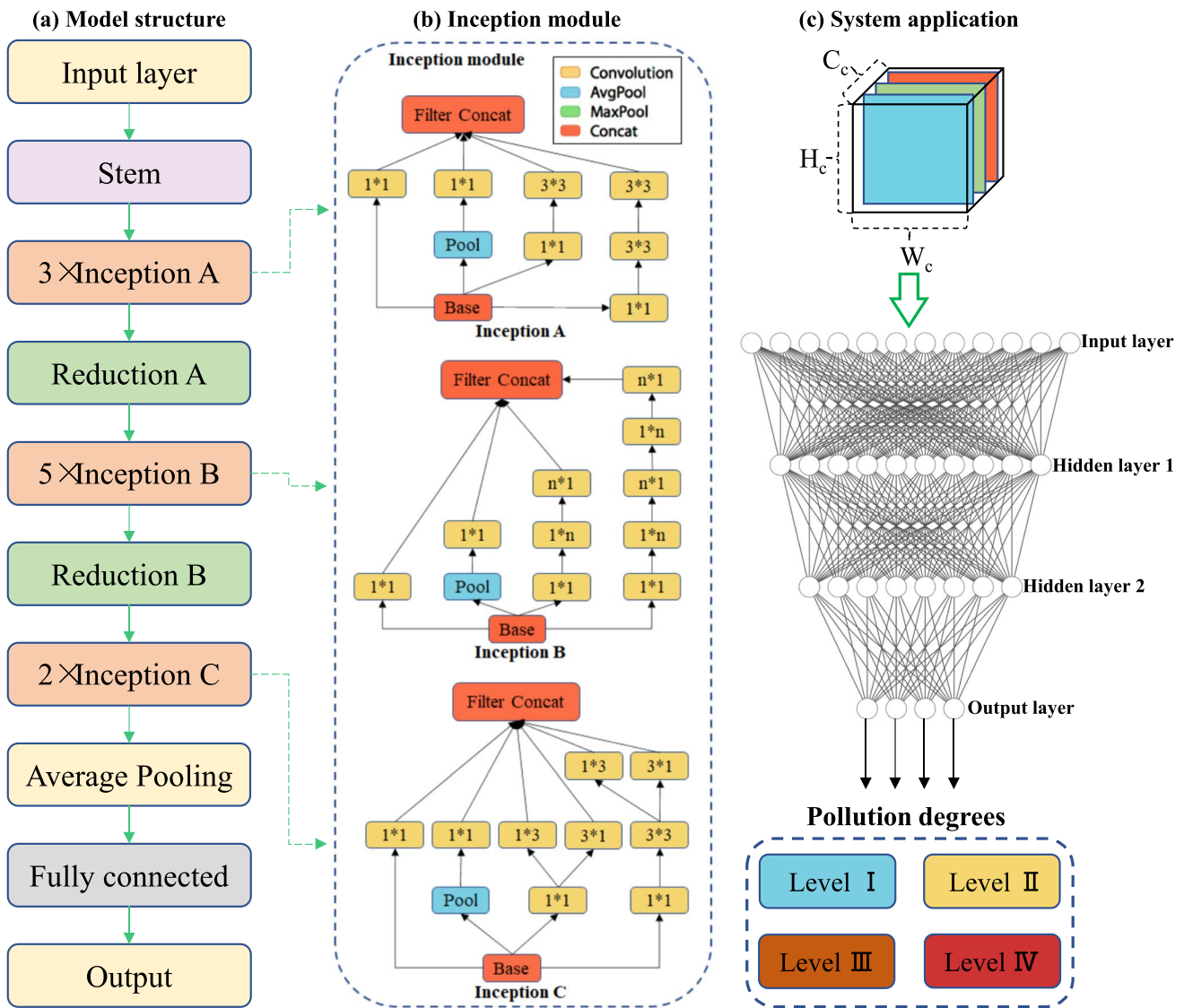
**Fig. 3** A schematic diagram of the proposed InceptionV3-based model, including **a** Model structure of the proposed DL framework, **b** The inception modules inside the model, and **c** System application with the input and output data

where $I^l(x+i-1, y+j-1, k)$ and $C_{W,b}^{l+1}(x, y)$ denote the convolutional input and output, respectively. $m$, $n$ represent the size of the convolutional kernel. $W_{i,j,k}^{l+1}$ is the weight coefficient for each convolutional kernel, and $bs$ is the bias vector. Regarding the global average pooling, $p^{l+1}(x, y)$ represents the pooling output of a single feature map, $x(p, q)$ is the element located at $(p, q)$ in the feature map area $R$.

Through the feature processing of the convolutional layer and pooling layer, the fully connected layer is applied as the final component of the hidden layer in the convolutional neural network. In this layer, the vectors $A = [a_1, a_2, \ldots, a_n]$ from the $l$th layer are subjected to a nonlinear combination of extracted features using a weight-coefficient matrix $W$ of size $n'*n$, and a bias matrix $B = [bs_1, bs_1,$

$\ldots, bs_{n'}]$ for the $(l+1)$th layer. The resulting feature graph loses its spatial topology in the fully connected layer and is expanded into vectors, which are then passed through an excitation function represented by Eq. (10). The fully connected layer can be mathematically expressed as Eq. (11):

$$f(x) = \tan h(x) = \frac{e^x - e^{-x}}{e^x + e^{-x}} \tag{10}$$

$$f_{n'}(x) = \tan h\left(\sum_{i=1}^{n} w_i x_i + bs_{n'}\right) \tag{11}$$

where $f_{n'}(x)$ denotes neurons of the output $(l+1)$th layer, and $i$ is the input neuron in the $l$th layer. n is the number of

**Fig. 4** The physical experiment system for dust image acquisition
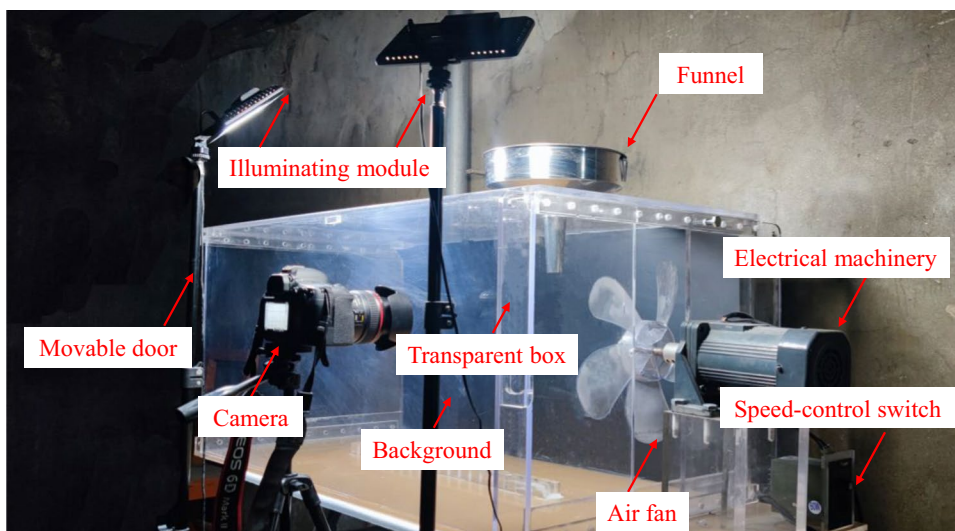


## 3 Dust diffusion simulation experiment for image acquisition

Dust dispersion often occurs in various production locations and is influenced by airflows of different wind speeds. In order to simulate and study the process of dust diffusion, a physical experiment system, depicted in Fig. 4, was designed to create a controlled dust diffusion environment. This system was specifically developed for capturing images of dust samples.

The entire system is comprised of three main modules: the dust generation module, which is responsible for producing dust samples; the air-flow control module, which ensures a stable airflow and controls the wind velocity; and the image acquisition module, which captures dust images and transfers them to the computer. The comprehensive overview of the system refers to Table 1. Additionally, the experimental procedures are shown as Fig. 5 and outlined below:

*Step one* begin by taking a specific amount of dolomite ash and drying it for 12 h to reduce the moisture content of dust particles, effectively mitigating adhesion. Subsequently, weigh the experimental sample using an electronic balance. For this experiment, three groups were prepared under the same conditions, ranging from 5 to 500 mg with a weighing interval of 5 mg.

*Step two* activate the fan to provide appropriate airflow, generating distinct dust dispersion. Adjust the fan speed to 800 r/min using the speed regulator. Then, initiate the camera and configure the parameters based on the particle characteristics and experimental environment. After

**Table 1** Equipment and materials for image acquisition

| Experimental subsystem | Composition/materials | Parameters |
|---|---|---|
| Dust generation module | Image acquisition box | Plexiglass with three leaks |
| | Funnel | Stainless steel $D_u$: 23 cm, $D_l$: 2.5 cm |
| | Dolomite ash | 74 µm/(10–300 mg) |
| | Dust dryer | JingHong DHG-9036A |
| | Electronic balance | FA 1004N |
| Air-flow control module | Electric motor | 220 V, 50 Hz |
| | Air fan | Five blades |
| | Speed regulator | 0–1200 r/min |
| Image acquisition module | Camera | Canon EOS 6D Mark II |
| | Illuminating apparatus | RUIMA RJ-10 LED 720 LUX,12 W |
| | ASUS Laptop | GeForce 2060, 32 GB |
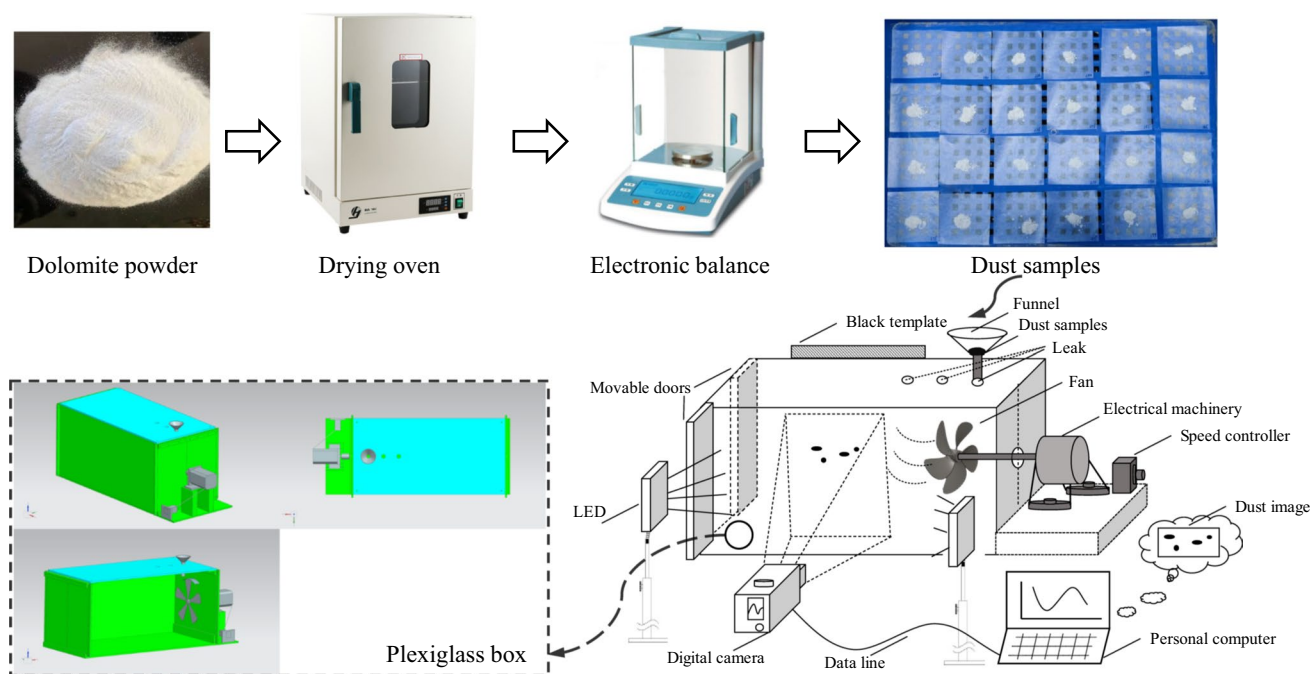
**Fig. 5** Schematic of the experiment procedures and equipment components

conducting multiple tests and optimizations, the camera parameters were determined as follows: shutter speed of 1/1000 s, ISO of 25600, and aperture of 4.0, respectively. In addition, LEDs with a color temperature of 5600 K and a light intensity of 720 LUX were utilized to ensure adequate illumination.

*Step three* pour the dust samples into the funnel containing a filter paper. Simultaneously, the camera starts capturing images for a duration of 3 s, with a time interval of 1/50 s between each capture. During the image acquisition period, the captured image data is wirelessly transmitted to the computer and subsequently processed using self-designed programs.

## 4 Results and discussion

### 4.1 GA and DF of dust images

After three groups of experiments, a total of 300 dust images were acquired and processed using the program. These images have a resolution of $1980 \times 1080$ pixels. Figure 6 below presents some sample images from the experiments along with their corresponding image-processing results.

From the Fig. 6, it demonstrates that the original images effectively capture the complete and legible diffusion trajectories of different quality dust samples weighing up to 500 mg. Then, through gradient calculation, the boundary characteristics of the dust particles are fairly recognized, so

that the ultimate binary feature images dramatically depict the macro quantitative relationship for different samples. Furthermore, the gradient calculations significantly reduce the adhesion phenomenon observed in dust clusters by removing the inner pixels. Thereafter, the grayscale averages of dust samples are calculated and depicted in Fig. 7. Additionally, linear fitting with the GA results was conducted, and the fitting equation along with goodness of fit ($R^2$) were also obtained.

According to the GA results presented in Fig. 7, $R^2$ for each group of dust samples is 0.49, 0.66 and 0.62, indicating a certain linear trend. However, upon examining the data distributions in the figure, it is evident that a few data points deviate from the expected pattern of development, resulting in significant data discreteness. This phenomenon can be attributed to the presence of unqualified dust images, which may have been influenced by improper timing of image capture and unfavorable environmental conditions such as air-flow speed and illuminant type. To mitigate the impact of data discreteness on particle characterization, Chauvenel criteria, an effective statistical method proposed to identify outliers, was adopted to improve the overall data analysis, and the mathematical expression is provided in Eq. (12).

$$\left| x_i - \bar{x} \right| > Z_c \hat{\sigma}(X) \tag{12}$$

where $x_i$ denotes the GA results, $Z_c$ is a coefficient that varies based on the number of tests n, $\bar{x}$ and $\hat{\sigma}(X)$ are the arithmetic

Original image ⟶ Gradient image ⟶ Gradient distribution ⟶ Binary image

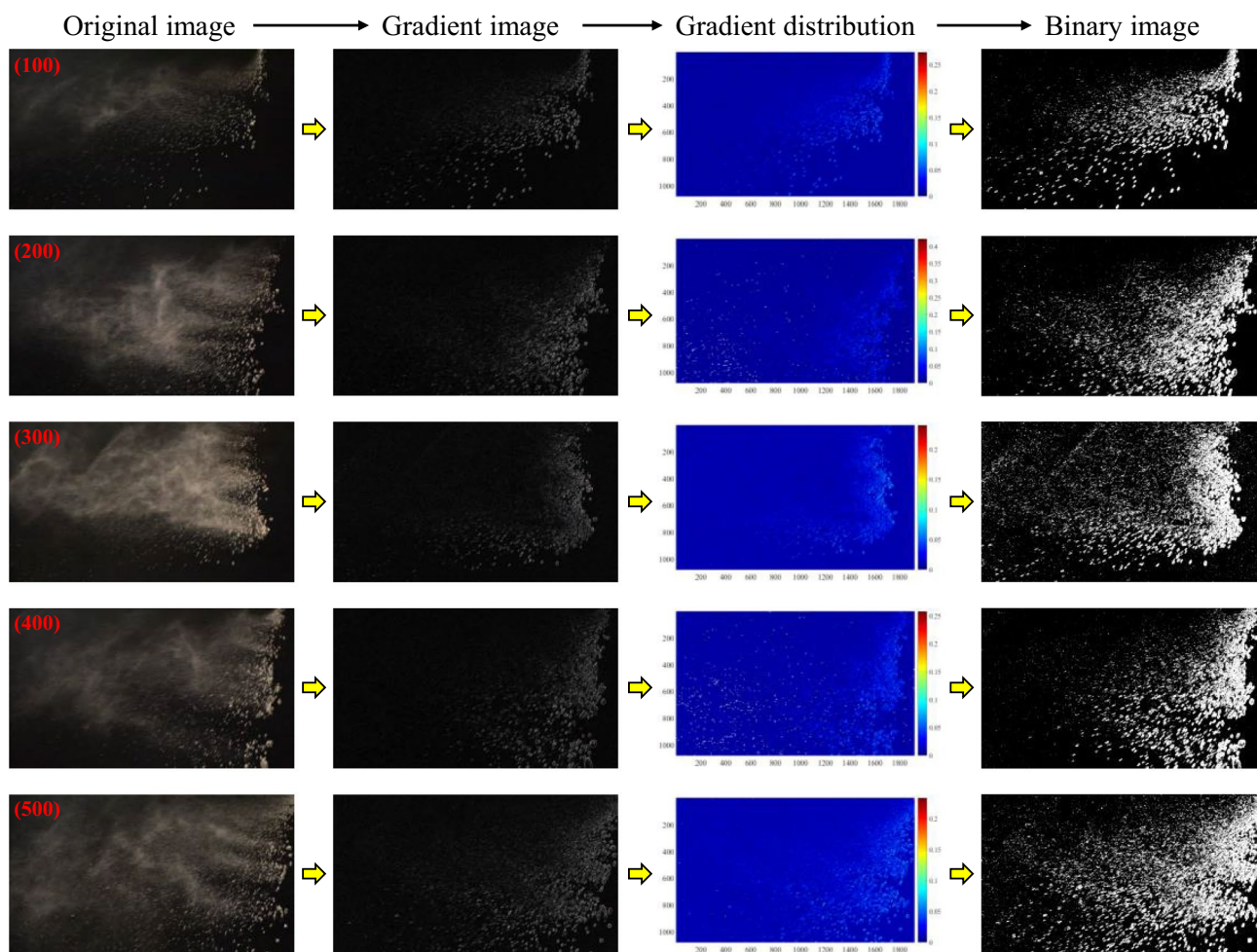**Fig. 6** Experimental dust images with the image processing results of 100 mg, 200 mg, 300 mg, 400 mg and 500 mg dust samples in group one
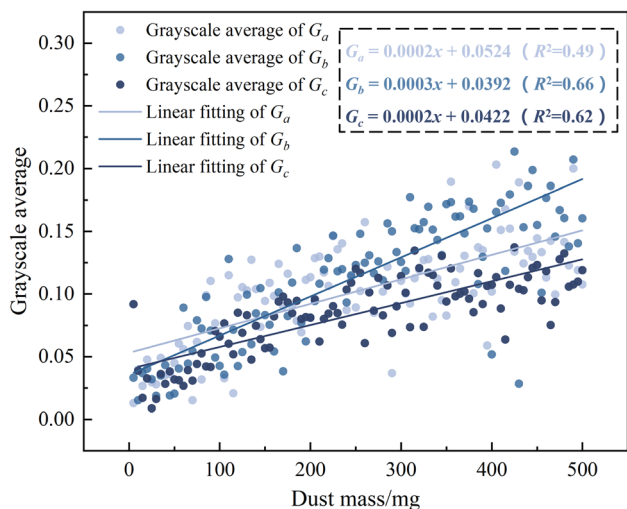
**Fig. 7** Grayscale averages of three-group dust samples, including the linear fitting results and homologous fitting equations

**Table 2** Dust masses of outliers within three groups

| Group number | Outliers of grayscale average (dust mass/ mg) |
|---|---|
| Group one | 290, 355, 395, 405 |
| Group two | 400, 430, 455 |
| Group three | 5, 25, 315, 415, 465 |

mean and standard deviation estimates of the image gray mean under the same conditions.

After applying the Chauvenet criteria for outlier detection, the outliers for each group were identified. Table 2 presents the detailed dust masses of these outliers. Subsequently, linear fitting was performed on the updated experimental data, and the resulting formula, along with the corresponding goodness of fit, is illustrated in Figs. 8a–c.
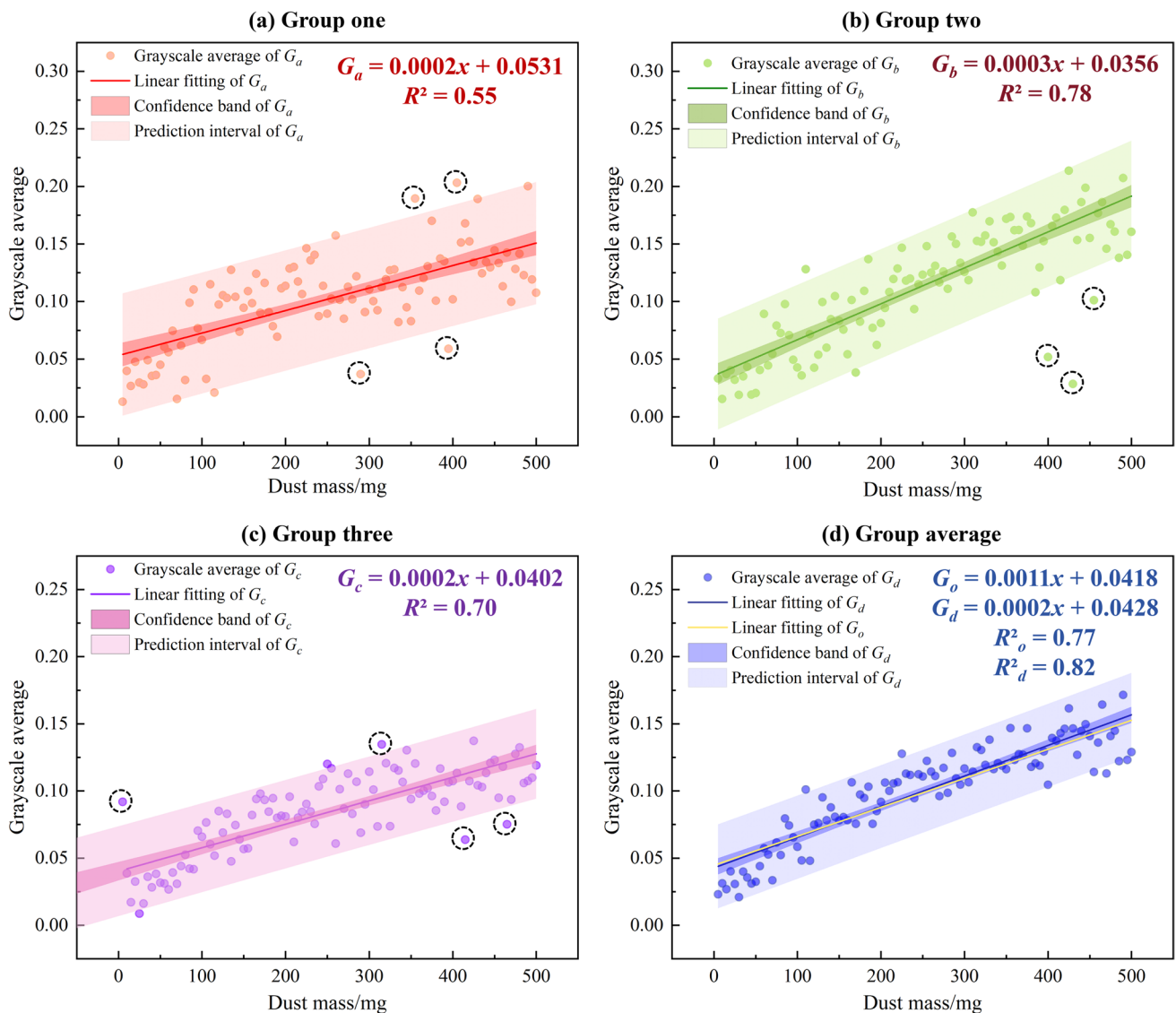
**Fig. 8** Grayscale-average results after removing outliers according to Chauvenel criteria, including **a** Grayscale averages of group one, **b** grayscale averages of group two, **c** Grayscale averages of group three, and **d** Grayscale averages of arithmetic-mean calculations of three groups

The outliers for each group are visually indicated by black-circle symbols. Additionally, the arithmetic mean of the GA results for the three groups was calculated. Linear fitting was then carried out both before and after the removal of outliers, as depicted in Fig. 8d.

It is evident from Figs. 8a–c that for each group, the outliers are identified through Chauvenel criteria. The linear relationships between GA and dust mass show significant improvement in goodness of fit values, increasing from 0.49, 0.66, and 0.62 to 0.55, 0.78, and 0.70, respectively. Meanwhile, to validate the effectiveness of the analysis, confidence bands and prediction intervals at a 95% level are employed. Compared to the image GA before outlier removal, most of the data points fall within the estimation intervals, especially within the confidence band. This

indicates that more data meets the estimation requirements at the confidence level. On the other hand, in Fig. 8d, the arithmetic average processing uniformly characterizes the three groups of GA, resulting in an ideal linear fit. Specifically, the linear fitting of GA data with outlier removal ($G_d$) exhibits a considerably increased goodness of fit ($R^2_d = 0.82$) compared to the original GA data ($G_o$) with $R^2_o$ as 0.77.

Regarding the fractal dimension of dust samples, outliers identified in Table 2 are also removed for each group. Subsequently, logarithmic fitting is performed to analyze the distribution pattern of the fractal dimension. The detailed calculations, fitting results, and associated confidence bands and prediction intervals are presented in Fig. 9.

From Figs. 9a–c, it can be observed that there is a certain degree of logarithmic relationship in the data distribution
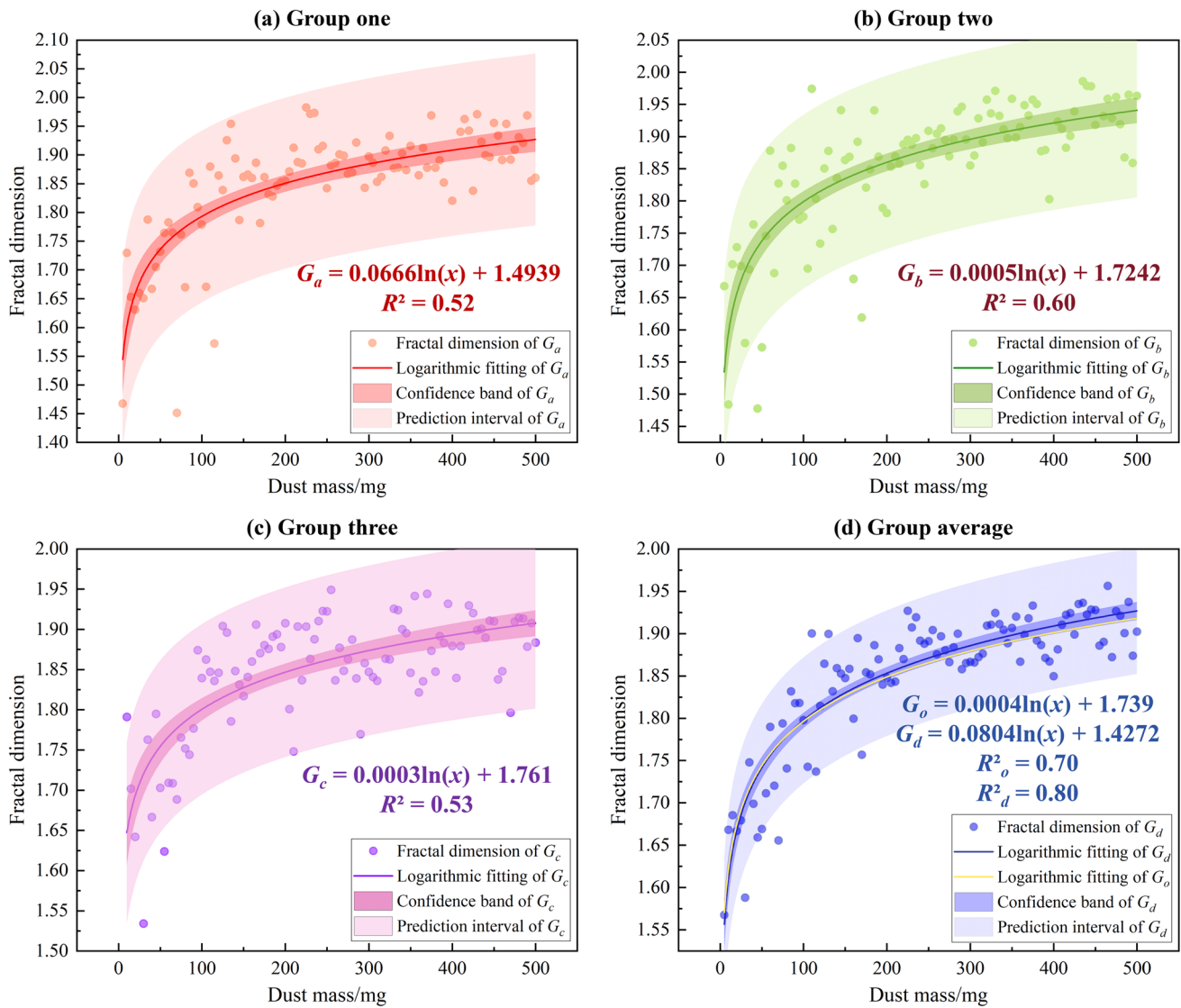
**Fig. 9** Fractal dimension results after outliers removal, including **a** Fractal dimensions of group one, **b** Fractal dimensions of group two, **c** Fractal dimensions of group three, and **d** Fractal dimensions of arithmetic-mean calculations of three groups

of the fractal dimension, as indicated by $R^2$ values of 0.52, 0.60, and 0.53 for each group. Despite the fact that outliers were removed prior to logarithmic fitting, there is still significant data discreteness within a single experimental group, with fractal dimension results exceeding the prediction interval. This discrepancy in fractal dimension data can be attributed to variations in the distribution pattern of dust diffusion, which is influenced by differences in dust mass. Through regressive analysis, the distribution of the fractal dimension is relatively scattered within the prediction interval and shows limited distribution within the confidence band. Nevertheless, the logarithmic correlation between fractal dimension and dust mass is ulteriorly improved when considering the arithmetic mean ($R^2_o = 0.70$), as shown in

Fig. 9d. The data discreteness is significantly reduced, with fractal dimension results converging within the prediction interval, particularly within the confidence band. Regarding outlier removal, the final expression $G_d$ provides a more reliable characterization of the fractal dimension of dust particles, achieving a goodness of fit of 0.80.

## 4.2 Hazardous index for preparing DL dataset

To comprehensively analyze the global and local features of a provided dust image, a hazardous index was proposed based on the image parameters of grayscale average and fractal dimension. The hazardous index formulation considers both the grayscale average (GA) and fractal dimension
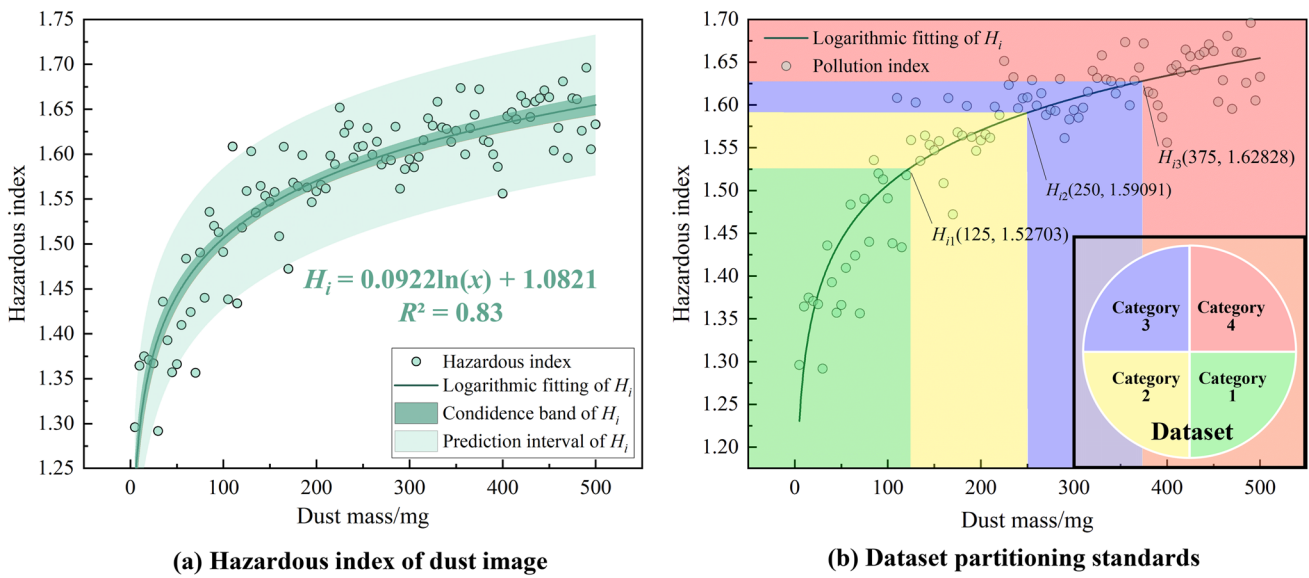
**(a) Hazardous index of dust image**    **(b) Dataset partitioning standards**

**Fig. 10** Hazardous index results for preparing the DL dataset, including **a** The hazardous index of the dust image consisting of homologous regressive analysis, and **b** Classification criteria for preparing the four-category DL dataset

(DF), weighting them based on the $R^2$ values of their respective mathematical expressions. Thus, the hazardous index $H_i$ can be denoted as Eq. (12), and the correlation with dust mass is also presented by Eq. (14) below. Based on Eq. (14), the hazardous index of the dust sample can be calculated, and the results are displayed in Fig. 10a. Additionally, the classification criteria for preparing the deep learning (DL) dataset are presented in Fig. 10b.

$$H_i = 0.82 \times DF + 0.80 \times GA \tag{13}$$

$$H_i = 0.0645 \ln(x) + 0.0002x + 1.1807 \tag{14}$$

Figure 10a illustrates the integration of global and local features of dust images, specifically the grayscale average and fractal dimension. It reveals a logarithmic relationship between the hazardous index and dust mass, exhibiting a quite fitting effect with a $R^2$ of 0.83. Meanwhile, the index

distribution within the confidence band and prediction interval indicates minimal data discreteness for the hazardous index.

Based on the regression equation of hazardous index, the value range of $H_i$ is [1.2304, 1.6548], corresponding to a dust-mass range of [5 mg, 500 mg]. Consequently, the dust images are divided into four categories in accordance with the $H_i$. The hazardous index ranges for each category are defined as follows: [1.2304, 1.3365] for category one, [1.3365, 1.4426] for category two, [1.4426, 1.5487] for category three, and [1.5487, 1.6548] for category four, respectively. For a reasonable consideration, $H_i$ values below 1.2304 and above 1.6548 are separately classified as category one and category four. Therefore, Fig. 10b illustrates that the $H_i$ values are separated into 22, 17, 24 and 37 data points for categories one to four, respectively.

**Table 3** Parameters and image results for data augmentation

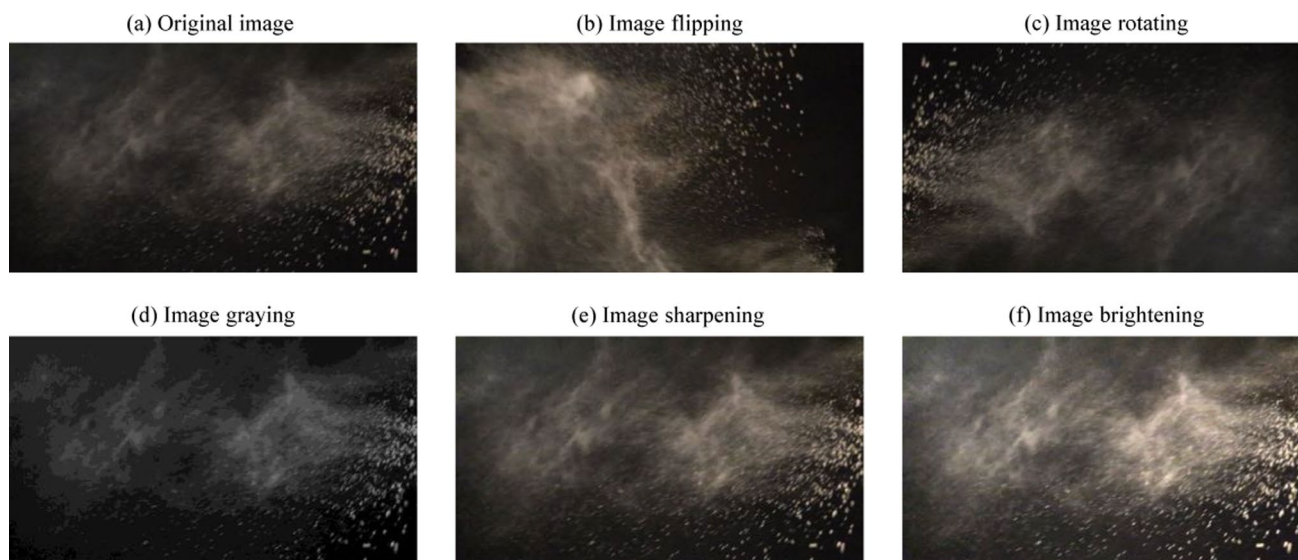| Image operations | Operation parameters | Image numbers | Total number |
|---|---|---|---|
| Flipping | Horizontal, vertical and diagonal | 900 | 4800 (include 300 original images) |
| Scaling | 0.25, 0.5, 2, 4 | 1200 | |
| Rotating | 90°, 180°, 270° | 900 | |
| Graying | – | 300 | |
| Sharpening | Sobel algorithm | 300 | |
| Brightening | 0.5, 1.5, 2.0 | 900 | |

**Fig. 11** Data augmentation processes, **a–f** represent original image, processing of flipping, rotating, graying, sharpening, and brightening, respectively

### 4.3 Dust risk classification system based on DL model

To prepare datasets for the DL model, several modifications were performed on the original set of 300 dust images. Random fluctuations in color temperature were applied to the images, and various data augmentation techniques, including flipping, scaling, rotating, graying, sharpening, and brightening, were employed. These techniques aimed to generate additional dust images and prevent overfitting caused by a limited dataset. Table 3 provides the selected parameters and the corresponding number of images for each operation. To visually illustrate the data augmentation processes, an image example from group one with a dust mass of 380 mg was selected. Figures 11a–f demonstrates some operations applied to this image.

Based on the results depicted in Fig. 10b, the four categories consist of 22, 17, 24 and 37 data points, respectively. Consequently, the training dataset for the model comprises 1056, 816, 1152, and 1776 dust images for each category. To ensure the model reliability, random sampling was utilized to select images for the training, validation, and testing sets. Specifically, 10% of the images were randomly allocated to the validation set, 10% to the testing set, and 80% to the training set.

Before commencing the model training, the neural network was initialized with a learning rate of 0.1, a batch size of 100, and 5000 steps. During the training process, the model parameters were continually updated by the gradient descent optimizer, while the cross-entropy function served as the loss function. To optimize subsequent training computations, the computed feature vectors were stored in a vector folder. These feature vectors, derived from dust images, could be utilized to exclude non-interest regions once the model was trained on a new dataset.

To evaluate the performance of the proposed model, the training and validation accuracy indices are utilized. These indices are calculated as the ratio of correctly classified samples to the total number of samples in the training and validation datasets, as depicted in Eq. (15). The training and validation accuracies are illustrated in Fig. 12a.

$$Training\ validation\ accuracy = \frac{n_{\text{true}}}{N_{\text{total}}} \tag{15}$$

Subsequently, to further evaluate the effectiveness of the proposed model, the testing accuracy is determined using a separate dataset comprising 970 dust images. This dataset includes 224 images from category one, 154 images from category two, 211 images from category three, and 381 images from category four. The true values and predicted values are presented in a confusion matrix, as shown in Fig. 12b. This matrix is essential in assessing the performance of the model by visually comparing the real and predicted categories. In the graph, categories one, two, three, and four are represented by the numbers 1, 2, 3, and 4, respectively. The testing accuracy can be obtained by calculating the true positive (TP), true negative (TN), false positive (FP), and false negative (FN) of each dust category, as described in Eq. (16).

$$Testing\ accuracy = \frac{TP + TN}{TP + TN + FP + FN} \tag{16}$$

**(a) Training and validation accuracy**    **(b) Confusion matrix**
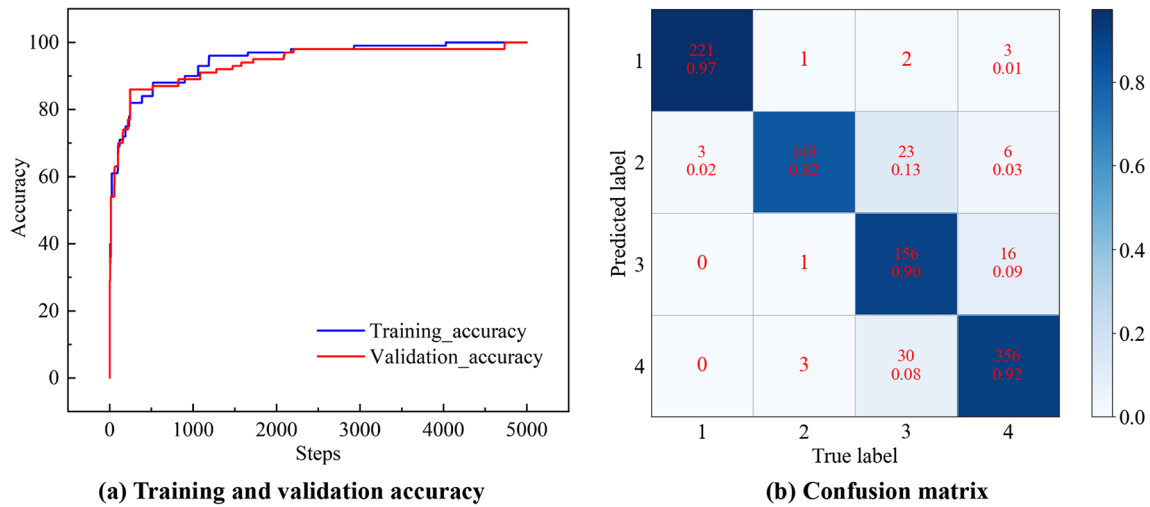
**Fig. 12** Training, validation, and testing performance, including **a** Training and validation accuracies, and **b** A normalized confusion matrix for the testing operation

where TP represents the number of correctly classified images from a certain dust category, while TN represents the number of correctly classified images from other dust categories. FP represents the number of erroneously classified images from other dust categories as the certain dust category, and FN represents the number of erroneously classified images from the certain dust category as other dust categories. The specific results are shown in Table 4.

Based on Table 4, the testing accuracy was calculated using a weighted mean method in accordance with the TP, TN, FP, and FN values of each category, and was found to be 95.3%.

The proposed framework depicted in Fig. 12a demonstrates a high degree of accuracy during the 5000 steps of training and validation, indicating the proper determination of the model parameters. However, fluctuations in the validation accuracy may occur due to variations in the dataset between each batch of training, validation, and testing. To evaluate the generalization capability of model, a separate testing dataset was employed, and Fig. 12b illustrates the comparison between the true and predicted values. The model performed well for most of the training data, but error rates increased with the number of dust samples. Ultimately, the model achieved a testing accuracy of 95.3%, indicating

its capability and reliability in classifying dust pollution levels.

Although validation is a valuable metric for evaluating a DL model, it may not provide detailed information on classification results. To address this limitation, three commonly used evaluation metrics for DL models were adopted in this network: precision, recall, and F1-score. The precision index represents the proportion of correctly predicted positive samples, the recall index indicates the proportion of actual positive samples correctly predicted, and the F1-score is a metric that combines both precision and recall. The expressions for these three indexes are:

$$\text{Precision} = \frac{\text{TP}}{\text{TP} + \text{FP}}, \ \text{Recall} = \frac{\text{TP}}{\text{TP} + \text{FN}},$$
$$F1 = \frac{2}{\frac{1}{P} + \frac{1}{R}} = \frac{2\text{TP}}{2\text{TP} + \text{FP} + \text{FN}} \quad (17)$$

Following the acquisition of each parameter, the evaluation of the proposed model was further carried out by calculating the weighted mean of the indexes. The results are summarized in Table 5. The findings reveal that the model exhibited a high level of accuracy in classifying dust pollution levels. Specifically, it demonstrated a high degree

**Table 4** Calculation results of TP, TN, FP, and FN based on the testing dataset

| True category | Prediction category I | Prediction category II | Prediction category III | Prediction category IV | TP | TN | FP | FN |
|---|---|---|---|---|---|---|---|---|
| Category I | 221 | 3 | 0 | 0 | 221 | 661 | 6 | 3 |
| Category II | 1 | 149 | 1 | 3 | 149 | 733 | 32 | 2 |
| Category III | 2 | 23 | 156 | 30 | 156 | 726 | 17 | 53 |
| Category IV | 3 | 6 | 16 | 356 | 356 | 526 | 30 | 25 |

**Table 5** Network precision, recall, and F1-score

| Indexes | Precision | Recall | F1-score |
|---|---|---|---|
| The proposed net | 0.9139 | 0.9138 | 0.9111 |

accuracy in of correctly predicting positive image samples and accurately identifying positive samples from the actual correct image samples. The F1-score, taking into account both precision and recall, also showed favorable performance. Overall, the proposed model proved to be accurate and dependable in assessing the degree of dust pollution.

The utilization of digital image processing and deep learning techniques in monitoring systems offers several benefits over traditional methods. These benefits encompass non-invasive operations, minimal equipment requirements, and more comprehensive and accurate monitoring. Moreover, the integration of these methods into existing control systems enables automated adjustments to ventilation and other control measures in real-time, thereby enhancing the efficiency and effectiveness of the system.

## 5 Conclusions

A comprehensive evaluation method is proposed based on an optimized image-processing method and a deep learning framework to analyze dust pollution generated in the production process of mines. The proposed method primarily utilizes digital images obtained through dust diffusion experiments to characterize the gray and fractal features within the images. Subsequently, a hazardous index is developed to integrate these two parameters to prepare a four-category dataset for the deep learning framework. This evaluation model enables the convenient acquisition and subsequent processing of dust pollution information at monitoring points. Based on the study, the following are the key findings:

(1) 300 dust images were acquired through the dust diffusion experiments and then processed by a series of image-processing operations. The parameter results of the grayscale average were also obtained and fitted. The results indicate a linear correlation between the grayscale average (GA) and dust mass, with $R^2$ of 0.49, 0.66 and 0.62 for each experimental group, respectively. To reduce the data discreteness, the Chauvenel criteria was adopted to remove outliers, resulting in updated $R^2$ of 0.55, 0.78 and 0.70. Particularly, by applying arithmetic average processing to the experimental groups, the $R^2$ of the final liner expression is improved to 0.82, demonstrating a reliable characterization of the relationship between gray features and dust quantity.

(2) Relevant calculations were conducted for the fractal dimension (DF), and outliers were also identified in line with the processing method as for GA. Further results denote a logarithmic correlation between the fractal dimension and dust mass, with $R^2$ of 0.52, 0.60 and 0.53 for the respective expressions. After removing outliers and applying arithmetic average processing, the $R^2$ is promoted to 0.80. Comparing the results of GA and DF, the fractal dimension exhibits more data discreteness, aligning with the applications of prediction interval and confidence band.

(3) A hazardous index is determined based on the GA and DF parameters, considering their respective fitting expressions and $R^2$. A logarithmic correlation is also obtained between the index and dust mass, with an $R^2$ value of 0.83 for the mathematical expression. Based on the hazardous index, dust images are divided into four categories according to the dust mass range. The $H_i$ range is [1.2304, 1.6548], corresponding to the dust-mass range [5 mg, 500 mg]. 22, 17, 24 and 37 data points for each category are acquired, serving as the partition criteria for the deep learning datasets.

(4) A dust risk classification system is established based on the deep learning model. A total of 4800 image datasets are achieved through a series of data augmentation techniques, with 1056, 816, 1152, and 1776 dust images determined for each category. During the model training process, training and validation accuracy are presented, demonstrating a high degree of performance after 5000 steps. Additionally, the testing accuracy is measured at 95.3%. Precision, recall, and F1-score are employed to further validate the model performance, resulting in final results of 0.9139, 0.9138, and 0.9111, respectively, confirming the reliability of the dust risk analysis system.

In conclusion, the vision-based method in this research offers advantages over traditional methods for dust pollution recognition and evaluation, including automation, objectivity, multidimensional analysis, real-time monitoring, and scalability. Its widespread application in scientific and technological domains has improved efficiency and accuracy in assessing dust pollution levels.

## 6 Future directions

Although progress has been made in dust identification, program design, parameter calculations, and image acquisition, there is a need for more research in this field. The proposed

image processing algorithm may be influenced by factors such as camera quality and dust sample types, requiring further parameter calibration research. The experimental system for dust diffusion would benefit from improvement in terms of verifiability and automation, necessitating careful design considerations for improved functionality. Additionally, the algorithm limitations, such as complex mine topography, need to be explored for effective application. Combining image processing with deep learning, a dust pollution evaluation system was developed, but it should be noted that further research on this topic will contribute to the development of application software and promote its use under engineering practice conditions.

**Author contributions** All the authors have given approval to the final version of the paper. JY and SW conducted the experiments, performed the softwares and manuscript writing; SW and JL carried out the manuscript rewriting and corrections, and provided funding acquisition; JL and KF carried out supervision and collaboration of the project.

**Data availability** The data used to support the findings of this study are available from the corresponding author upon request.

## Declarations

**Conflict of interest** The authors declare no competing interests.

**Ethical approval** The research does not report on or involve the use of any animal or human data or tissue.

## References

Albatayneh O, Forslöf L, Ksaibati K (2019) Developing and validating an image processing algorithm for evaluating gravel road dust. Int J Pav Res Technol 12(3):288–296

Albatayneh O, Forslof L, Ksaibati K (2020) Image retraining using TensorFlow implementation of the pretrained inception-v3 model for evaluating gravel road dust. J Infrastruct Syst 26(2):04020014

Bao Q, Nie W, Liu C, Zhang H, Wang H, Jin H (2020) The preparation of a novel hydrogel based on crosslinked polymers for suppressing coal dusts. J Clean Prod 249:119343

Cai M (2019) Rock support in strainburst-prone ground. Int J Min Sci Technol 29(4):529–534

Chen D, Nie W, Cai P, Liu Z (2018) The diffusion of dust in a fully-mechanized mining face with a mining height of 7 m and the application of wet dust-collecting nets. J Clean Prod 205:463–476

Chen X, Li L, Wang L, Qi L (2019) The current situation and prevention and control countermeasures for typical dynamic disasters in kilometer-deep mines in China. Saf Sci 115:229–236

Conesa HM, Faz Á, Arnaldos R (2006) Heavy metal accumulation and tolerance in plants from mine tailings of the semiarid Cartagena-La Unión mining district (SE Spain). Sci Total Environ 366(1):1–11

Cyrys J, Dietrich G, Kreyling W, Tuch T, Heinrich J (2001) PM2.5 measurements in ambient aerosol: comparison between Harvard impactor (HI) and the tapered element oscillating microbalance (TEOM) system. Sci Total Environ 278(1–3):191–197

Fan L, Liu S (2021) Respirable nano-particulate generations and their pathogenesis in mining workplaces: a review. Int J Coal Sci Technol 8(2):179–198

Fu Y, Wang N (2013) Measurement of dust concentration based on VBAI. J Phys Conf Ser 418(1):12079

Grasa G, Abanades JC (2001) A calibration procedure to obtain solid concentrations from digital images of bulk powders. Powder Technol 114(1):125–128

He MC (2009) Application of HEMS cooling technology in deep mine heat hazard control. Min Sci Technol 19(3):269–275

Hill W, Lim EL, Weeden CE, Lee C, Augustine M, Chen K (2023) Lung adenocarcinoma promotion by air pollutants. Nature 616(7955):159–167

Hosseini S, Monjezi M, Bakhtavar E, Mousavi A (2021) Prediction of dust emission due to open pit mine blasting using a hybrid artificial neural network. Nat Resour Res 30(6):4773–4788

Ji Y, Ren T, Wynne P, Wan Z, Ma Z, Wang Z (2016) A comparative study of dust control practices in Chinese and Australian longwall coal mines. Int J Min Sci Technol 26(2):199–208

Lépy M, Cassette P, Ferreux L (2010) Measurement of beta-plus emitters by gamma-ray spectrometry. Appl Radiat Isot 68(7–8):1423–1427

Li G, Wu J, Luo Z, Chen X (2019) Vision-based measurement of dust concentration by image transmission. IEEE Trans Instrum Meas 68(10):3942–3949

Liang C, Lai C, Wang S, Lin Y (2021) Environmental microorganism classification using optimized deep learning model. Environ Sci Pollut Res Int 28(24):31920–31932

Lim KS, Gururajan VS, Agarwal PK (1993) Mixing of homogeneous solids in bubbling fluidized beds: theoretical modelling and experimental investigation using digital image analysis. Chem Eng Sci 12(48):2251–2265

Liu T, Liu S (2020) The impacts of coal dust on miners' health: a review. Environ Res 190:109849

Miguel A, Felipe G, Andrew F, Ashray D (2015) Towards the development of a low cost airborne sensing system to monitor dust particles after blasting at open-pit mine sites. Sensors 15(8):19667–19687

Obregón L, Velázquez C (2007) Discrimination limit between mean gray values for the prediction of powder concentrations. Powder Technol 175(1):8–13

Qi C, Zhou W, Lu X, Luo H, Pham BT, Yaseen ZM (2020) Particulate matter concentration from open-cut coal mines: a hybrid machine learning estimation. Environ Pollut 263:114517

Shekarian Y, Rahimi E, Shekarian N, Rezaee M, Roghanchi P (2021) An analysis of contributing mining factors in coal workers' pneumoconiosis prevalence in the United States coal mines, 1986–2018. Int J Coal Sci Technol 8(6):11

Shirmohammadi S, Ferrero A (2014) Camera as the instrument: the rising trend of vision based measurement. IEEE Instrum Meas Mag 3(17):7

Tan B, Liu H, Xu B, Wang T (2020) Comparative study of the explosion pressure characteristics of micro- and nano-sized coal dust and methane-coal dust mixtures in a pipe. Int J Coal Sci Technol 7(1):68–78

Tong R, Cheng M, Yang X, Yang Y, Shi M (2019) Exposure levels and health damage assessment of dust in a coal mine of Shanxi Province, China. Process Saf Environ Prot 128:184–192

Valiulin SV, Onischuk AA, Baklanov AM, Bazhina AA, Paleev DY, Zamashchikov VV (2020) Effect of coal mine organic aerosol on the methane/air lower explosive limit. Int J Coal Sci Technol 7(4):9

Wang H, Wang C, Wang D (2017) The influence of forced ventilation airflow on water spray for dust suppression on heading face in underground coal mine. Powder Technol 320:498–510

Wang S, Yin J, Liang Y, Tian F (2022) Dust pollution evaluation based on grayscale average and fractal dimension of digital image. J Clean Prod 379:134691. https://doi.org/10.1016/j.jclepro.2022.134691

Yin J, Lu J, Tian F, Wang S (2022) Pollutant migration pattern during open-pit rock blasting based on digital image analysis technology. Mathematics 10(17):3205

Zhang L, Wang J, Feng Y (2018) Life cycle assessment of opencast coal mine production: a case study in Yimin mining area in China. Environ Sci Pollut Res Int 25(9):8475–8486

Zhang H, Nie W, Liang Y, Chen J, Peng H (2021) Development and performance detection of higher precision optical sensor for coal dust concentration measurement based on Mie scattering theory. Opt Lasers Eng 144:106642

Zhou G, Fan T, Ma Y (2017a) Preparation and chemical characterization of an environmentally-friendly coal dust cementing agent. J Chem Technol Biotechnol 92(10):2699–2708

Zhou G, Zhang Q, Bai R, Fan T, Wang G (2017b) The diffusion behavior law of respirable dust at fully mechanized caving face in coal mine: CFD numerical simulation and engineering application. Process Saf Environ Prot 106:117–128